



Polarimetric SAR characterization of man-made structures in urban areas using normalized circular-pol correlation coefficients

T.L. Ainsworth*, D.L. Schuler, J.-S. Lee

Remote Sensing Division, Naval Research Laboratory, Washington, DC 20375-5351, USA

ARTICLE INFO

Article history:

Received 2 August 2007

Received in revised form 1 February 2008

Accepted 2 February 2008

Keywords:

Polarimetric SAR

Urban Area Detection

Circular-pol Correlation Coefficient

Target Detection

ABSTRACT

Polarimetric Synthetic Aperture Radar (SAR) backscatter from man-made structures in urban areas is quite different than backscatter from predominantly natural areas. Backscatter from natural areas is often reflection symmetric; i.e., characterized by near zero values for covariance matrix off-diagonal terms of the form $\langle S_{HV}S_{HH}^* \rangle$, $\langle S_{HV}S_{VV}^* \rangle$ and their conjugates. A new approach is proposed to detect scattering from non-reflection symmetric structures using circular-pol, RR-LL, correlation coefficients, $|\rho|$. This method creates a normalization term, $|\rho_0|$, and then forms a ratio, $|\rho|/|\rho_0|$. The normalization term, $|\rho_0|$, contains the same diagonal terms of the covariance matrix. The $\langle S_{HV}S_{HH}^* \rangle$ and $\langle S_{HV}S_{VV}^* \rangle$ off-diagonal terms and their conjugates are purposely set to zero. The ratio, $|\rho|/|\rho_0|$, is rewritten as a product of separable helicity (τ) and orientation angle (θ) dependencies. The mathematical form of the τ dependence is a resonant singularity, or pole, term. This pole significantly enhances returns from man-made, high helicity, non-reflection symmetric structures. These structures have values of τ near the resonance value at $\tau = \pm 1$. Natural scatterers possess very strong RR / LL symmetry ($\tau = 0$) and the pole response for them is correspondingly weak. The dependence of $|\rho|/|\rho_0|$ on the orientation angle (θ) is known from previous studies to be useful for measuring urban building alignments (relative to the azimuth direction) and measuring surface topography. The ratio $|\rho|/|\rho_0|$ reduces much of the un-needed image detail of backscatter variations from natural areas of different surface roughness. This image simplification further facilitates detection of localized man-made targets.

Published by Elsevier Inc.

1. Introduction

Segmentation of scatter from man-made structures in urban areas and scatter from surrounding natural targets remains important for polarimetric Synthetic Aperture Radar (SAR) terrain categorization and image classification. Buildings and other man-made structures primarily aligned in the along-track direction are relatively easy to detect by their strong double-bounce and/or specular polarimetric scattering characteristics and weak cross-pol returns. Both double-bounce and specular scattering obey reflection symmetry, the lack of coherence between the linear co-pol and cross-pol returns; i.e., $\langle S_{HV}S_{HH}^* \rangle = \langle S_{HV}S_{VV}^* \rangle = 0$, where S_{HH} , S_{HV} , etc., are the scattering matrix elements. However, backscatter from man-made structures in urban areas also occurs from complex geometries and, therefore, reflection symmetry is often broken. The covariance matrix mixed polarization terms (e.g., $\langle S_{HV}S_{HH}^* \rangle$, $\langle S_{HV}S_{VV}^* \rangle$ and their conjugates) can be quite

large for these scattering cases. Structures that are not aligned to the flight path, or are positioned on sloping terrain, induce significant cross-pol backscatter and lack reflection symmetry. Here we address the problem of detecting and segmenting man-made structures in these more complicated situations.

An investigation involving the detection properties of circular-pol, RR-LL, correlation coefficient, $|\rho|$, images has been carried out. The effort was to increase the sensitivity for detecting man-made structures, which are embedded in a natural background of reflection symmetric scatterers.

In the approach described here, the conventional RR-LL correlation coefficient, $|\rho|$, is normalized by a circular-pol RR-LL correlation coefficient, $|\rho_0|$, constructed from the same covariance matrix terms, but with the mixed terms, $\langle S_{HV}S_{HH}^* \rangle$, $\langle S_{HV}S_{VV}^* \rangle$, artificially set to zero (reflection symmetric case). This new method produces large values for the ratio $|\rho|/|\rho_0|$ when the condition of reflection symmetry is violated.

For multi-look scattering the polarimetric covariance C matrix is given by:

$$[C] = \begin{bmatrix} \langle |S_{HH}|^2 \rangle & \langle \sqrt{2} S_{HH}S_{HV}^* \rangle & \langle S_{HH}S_{VV}^* \rangle \\ \langle \sqrt{2} S_{HV}S_{HH}^* \rangle & \langle 2|S_{HV}|^2 \rangle & \langle \sqrt{2} S_{HV}S_{VV}^* \rangle \\ \langle S_{VV}S_{HH}^* \rangle & \langle \sqrt{2} S_{VV}S_{HV}^* \rangle & \langle |S_{VV}|^2 \rangle \end{bmatrix} \quad (1)$$

* Corresponding author. Code 7263, Remote Sensing Division, Naval Research Laboratory, Washington, DC 20375-5351, USA. Tel.: +1 202 404 6369.

E-mail address: ainsworth@nrl.navy.mil (T.L. Ainsworth).

where the $\langle \dots \rangle$ indicates the ensemble average. The S_{HH} , S_{HV} , etc. are the scattering matrix elements. The full covariance matrix Eq. (1) determines the conventional RR-LL correlation coefficient, $|\rho|$. Forcing reflection symmetry in Eq. (1) by artificially setting matrix elements $C_{12}=C_{21}=C_{23}=C_{32}=0$ defines the normalized RR-LL correlation coefficient, $|\rho_0|$. Therefore, for reflection symmetric scattering, the ratio, $|\rho|/|\rho_0|$, is one since both linear co-pol / cross-pol correlations are already zero.

The proposed circular-pol correlation ratio, $|\rho|/|\rho_0|$, averages to one, or nearly one, in flat natural terrain areas. The ratio has larger values for scattering from man-made structures (Schuler et al., 2006a,b). Previous studies; e.g., (Kimura et al., 2004, 2005), showed the effects of urban structure wall-alignments on the polarimetric orientation angle. The orientation angles in the urban areas were simultaneously influenced, however, by changes in orientation of ground topography. Kimura et al. (2005) introduced a scattering model for urban areas incorporating both single and double bounce scattering. Where their scattering model applies, they used $\text{Arg}(\langle S_{HV}S_{HH}^* \rangle)$ and the rotation of buildings in the scene to identify regions of primarily single or double bounce scattering. They found double bounce scattering predominates in the urban areas of their study. By design the ratio $|\rho|/|\rho_0|$ is sensitive to the linear co-pol/cross-pol correla-

tions, e.g. $\langle S_{HV}S_{HH}^* \rangle$, though it does not separate single from double bounce scattering. The correlation ratio, $|\rho|/|\rho_0|$, provides a means to separate scatter from man-made structures versus scatter from natural areas and ultimately to segment the return into these distinct scattering classes.

2. Normalization of circular RR-LL correlation coefficients

The correlation coefficient, ρ_{aabb} , for the co-pol case can be expressed as:

$$\rho_{aabb} = \frac{\langle S_{aa}S_{bb}^* \rangle}{\sqrt{\langle S_{aa}S_{aa}^* \rangle} \sqrt{\langle S_{bb}S_{bb}^* \rangle}} \tag{2}$$

Circular-pol images using the correlation coefficient ρ_{RRLL} (a=R: right-circular polarization; b=L: left-circular polarization) were created as shown in Eq. (3). We developed the circular-pol normalization proposed in this study to reduce the effects of scattering terms that are associated with natural areas and simultaneously to enhance the return from man-made structures. Generally, a 5×5 ensemble average is used to form $|\rho|/|\rho_0|$.

3. Derivation of a RR-LL normalized correlation ratio, $|\rho|/|\rho_0|$, as a function of helicity (τ) and orientation angle (θ)

To derive $|\rho|/|\rho_0|$ as a function of helicity τ and orientation angle θ , we introduce the general form of the RR-LL correlation coefficient and then give the definition of the circular polarization basis with respect to the linear basis, and vice versa. Specifically,

$$\rho_{RRLL} = \frac{\langle S_{RR}S_{LL}^* \rangle}{\sqrt{\langle S_{RR}S_{RR}^* \rangle} \sqrt{\langle S_{LL}S_{LL}^* \rangle}} \tag{3}$$

The transformation from the linear to circular basis is as follows:

$$\begin{aligned} S_{RR} &= iS_{HV} + \frac{1}{2}(S_{HH} - S_{VV}) \\ S_{LL} &= iS_{HV} - \frac{1}{2}(S_{HH} - S_{VV}) \end{aligned} \tag{4}$$

which when substituted into Eq. (3) yields,

$$\rho_{RRLL} = \frac{-\left\langle \left| \frac{S_{HH}-S_{VV}}{2} \right|^2 - |S_{HV}|^2 + 2i\Re\left(S_{HV}^* \left(\frac{S_{HH}-S_{VV}}{2} \right) \right) \right\rangle}{\sqrt{\left\langle \left| \frac{S_{HH}-S_{VV}}{2} \right|^2 + |S_{HV}|^2 + 2\Im\left(S_{HV}^* \left(\frac{S_{HH}-S_{VV}}{2} \right) \right) \right\rangle} \cdot \left\langle \left| \frac{S_{HH}-S_{VV}}{2} \right|^2 + |S_{HV}|^2 - 2\Im\left(S_{HV}^* \left(\frac{S_{HH}-S_{VV}}{2} \right) \right) \right\rangle}} \tag{5}$$

The symbols $\Re(X)$ and $\Im(X)$ denote the real and imaginary parts of X , respectively. The first observation concerning Eq. (5) involves the phase of the complex-valued, ρ_{RRLL} . The denominator is real; therefore, the ratio of the imaginary part to the real part of the numerator in Eq. (5) determines the orientation angle via Lee et al. (2000, 2002) as:

$$\tan(4\theta) = \frac{-2\Re\left(\left\langle S_{HV}^* \left(\frac{S_{HH}-S_{VV}}{2} \right) \right\rangle \right)}{\left\langle \left| \frac{S_{HH}-S_{VV}}{2} \right|^2 - |S_{HV}|^2 \right\rangle} \tag{6}$$

Secondly, the equation for ρ_0 is straightforwardly derived from Eq. (5) as:

$$\rho_0 = \frac{-\left\langle \left| \frac{S_{HH}-S_{VV}}{2} \right|^2 - |S_{HV}|^2 \right\rangle}{\sqrt{\left\langle \left| \frac{S_{HH}-S_{VV}}{2} \right|^2 + |S_{HV}|^2 \right\rangle} \cdot \left\langle \left| \frac{S_{HH}-S_{VV}}{2} \right|^2 + |S_{HV}|^2 \right\rangle}} \tag{7}$$

The ratio $|\rho|/|\rho_0|$ may be written using Eqs. (5) and (7) as:

$$\begin{aligned} \left| \frac{\rho_{RRLL}}{\rho_0} \right| &= \frac{\left| \left\langle \left| \frac{S_{HH} - S_{VV}}{2} \right|^2 - |S_{HV}|^2 + 2i\Re \left(S_{HV}^* \left(\frac{S_{HH} - S_{VV}}{2} \right) \right) \right\rangle \right|}{\left| \left\langle \left| \frac{S_{HH} - S_{VV}}{2} \right|^2 - |S_{HV}|^2 \right\rangle \right|} \\ &= \frac{\sqrt{\left\langle \left| \frac{S_{HH} - S_{VV}}{2} \right|^2 + |S_{HV}|^2 \right\rangle} \cdot \left\langle \left| \frac{S_{HH} - S_{VV}}{2} \right|^2 + |S_{HV}|^2 \right\rangle}{\sqrt{\left\langle \left| \frac{S_{HH} - S_{VV}}{2} \right|^2 + |S_{HV}|^2 + 2\Im \left(S_{HV}^* \left(\frac{S_{HH} - S_{VV}}{2} \right) \right) \right\rangle} \cdot \left\langle \left| \frac{S_{HH} - S_{VV}}{2} \right|^2 + |S_{HV}|^2 - 2\Im \left(S_{HV}^* \left(\frac{S_{HH} - S_{VV}}{2} \right) \right) \right\rangle} \\ &= \left\{ 1 + \frac{4\Re \left(\left\langle S_{HV}^* \left(\frac{S_{HH} - S_{VV}}{2} \right) \right\rangle \right)^2}{\left(\left\langle \left| \frac{S_{HH} - S_{VV}}{2} \right|^2 - |S_{HV}|^2 \right\rangle \right)^2} \right\}^{1/2} \cdot \left\{ 1 - \frac{4\Im \left(\left\langle S_{HV}^* \left(\frac{S_{HH} - S_{VV}}{2} \right) \right\rangle \right)^2}{\left(\left\langle \left| \frac{S_{HH} - S_{VV}}{2} \right|^2 + |S_{HV}|^2 \right\rangle \right)^2} \right\}^{-1/2} \end{aligned} \quad (8)$$

Employing Eq. (6) for the orientation angle term simplifies the first bracketed term in the last line of Eq. (8). The definitions of the Stokes matrix parameters m_{11} , m_{14} , and m_{44} given in Eq. (9) reduce the second term of Eq. (8).

$$\begin{aligned} m_{11} &= 0.25 \cdot [(S_{HH} \cdot S_{HH}^*) + (S_{VV} \cdot S_{VV}^*) + 2(S_{HV} \cdot S_{HV}^*)] \\ m_{14} &= 0.5 \cdot [\Im(S_{HH}^* \cdot S_{HV}) + \Im(S_{HV}^* \cdot S_{VV})] \\ m_{44} &= 0.5 \cdot [(S_{HV} \cdot S_{HV}^*) - \Re(S_{HH}^* \cdot S_{VV})] \end{aligned} \quad (9)$$

Dropping the implied absolute value signs yields:

$$\left| \frac{\rho}{\rho_0} \right| = \{1 + \tan^2(4\theta)\}^{1/2} \cdot \left\{ 1 - \left(\frac{2\langle m_{14} \rangle}{\langle m_{11} \rangle + \langle m_{44} \rangle} \right)^2 \right\}^{-1/2} \quad (10)$$

This form is convenient when working with compressed multi-looked NASA/JPL Airborne Synthetic Aperture Radar (AIRSAR) data, which is stored in Stokes matrix format.

An alternate form results when the second term of the last line in Eq. (8) is rewritten using Eq. (4) in terms of circular basis covariance matrix elements as:

$$\left| \frac{\rho}{\rho_0} \right| = \{1 + \tan^2(4\theta)\}^{1/2} \cdot \left\{ 1 - \left(\frac{\langle |S_{RR}|^2 \rangle - \langle |S_{LL}|^2 \rangle}{\langle |S_{RR}|^2 \rangle + \langle |S_{LL}|^2 \rangle} \right)^2 \right\}^{-1/2} = \sqrt{\frac{1 + \tan^2(4\theta)}{1 - \tau^2}} \quad (11)$$

where the expression for τ is:

$$\tau = \frac{\langle |S_{RR}|^2 \rangle - \langle |S_{LL}|^2 \rangle}{\langle |S_{RR}|^2 \rangle + \langle |S_{LL}|^2 \rangle} \quad (12)$$

In this form, $|\rho|/|\rho_0|$ highlights the role of τ in the scattering mechanisms. The connection between τ , defined in Eq. (12), and helicity is developed in the Appendix. Helicity appears as an asymmetry between the relative strengths of the $|S_{RR}|^2$ and $|S_{LL}|^2$ covariance matrix terms. Values of τ range between $[-1, +1]$. Typically, but not always, natural scatterers possess very little RR/LL asymmetry; i.e., $\tau \approx 0$. The $|\rho|/|\rho_0|$ ratio utilizes the singularity (at, or near, $|\tau|=1$) of Eq. (11) for non-reflection symmetric scatterers where often $|\tau| \approx 1$ and these returns are selectively made stronger in the image. The derivation for the value of the orientation angle (θ) in circular-pol covariance matrix terms is given in Lee et al. (2000, 2002).

In surface scatter cases, unwanted roughness details can be eliminated from images. For the case of reflection symmetry, Mattia et al. (1997) showed that $|\rho|$ is of the form:

$$|\rho| = \frac{\langle |S_{HH} - S_{VV}|^2 - 4|S_{HV}|^2 \rangle}{\langle |S_{HH} - S_{VV}|^2 + 4|S_{HV}|^2 \rangle} \quad (13)$$

This expression is proved to be highly sensitive to surface roughness (Kasilingam et al., 2001). This sensitivity causes circular-pol, $|\rho|$, images to contain a lot of detail about surface roughness spatial variation. The normalization algorithm eliminates many surface roughness details from the image by forming the ratio $|\rho|/|\rho_0|$.

4. Discussion of properties of the ratio $|\rho|/|\rho_0|$

A new theoretical expression for $|\rho|/|\rho_0|$ has been developed in the previous section (Eq. (11)). The value of $|\rho|/|\rho_0|$ is a function of both helicity (τ) and polarimetric orientation angle (θ). The structure of Eq. (11) may be written as the product of two independent functions as follows:

$$|\rho|/|\rho_0| = f(\tau) \cdot g(\theta). \quad (14)$$

Where $f(\tau)$ is calculated either from Stokes parameters, Eq. (10), or from circular basis scattering matrix elements, Eq. (12). The function $g(\theta)$

is a function of the orientation angle calculated from Eq. (6), or equivalently from the $\text{Arg}(|S_{RR} \cdot S_{LL}^*|)$.

$$\begin{aligned} g(\theta) &= \sqrt{1 + \tan^2(4\theta)} = \sec(4\theta) \\ f(\tau) &= [1 - \tau^2]^{-1/2} \end{aligned} \quad (15)$$

Helicity is, by itself, an important indicator of complex scattering from urban structures. In urban areas helicity is aspect angle and scale dependent. Touzi (2007), as an example, has determined

that helicity is required for the assessment of the symmetry–asymmetry nature of target scattering from complex structures in urban areas.

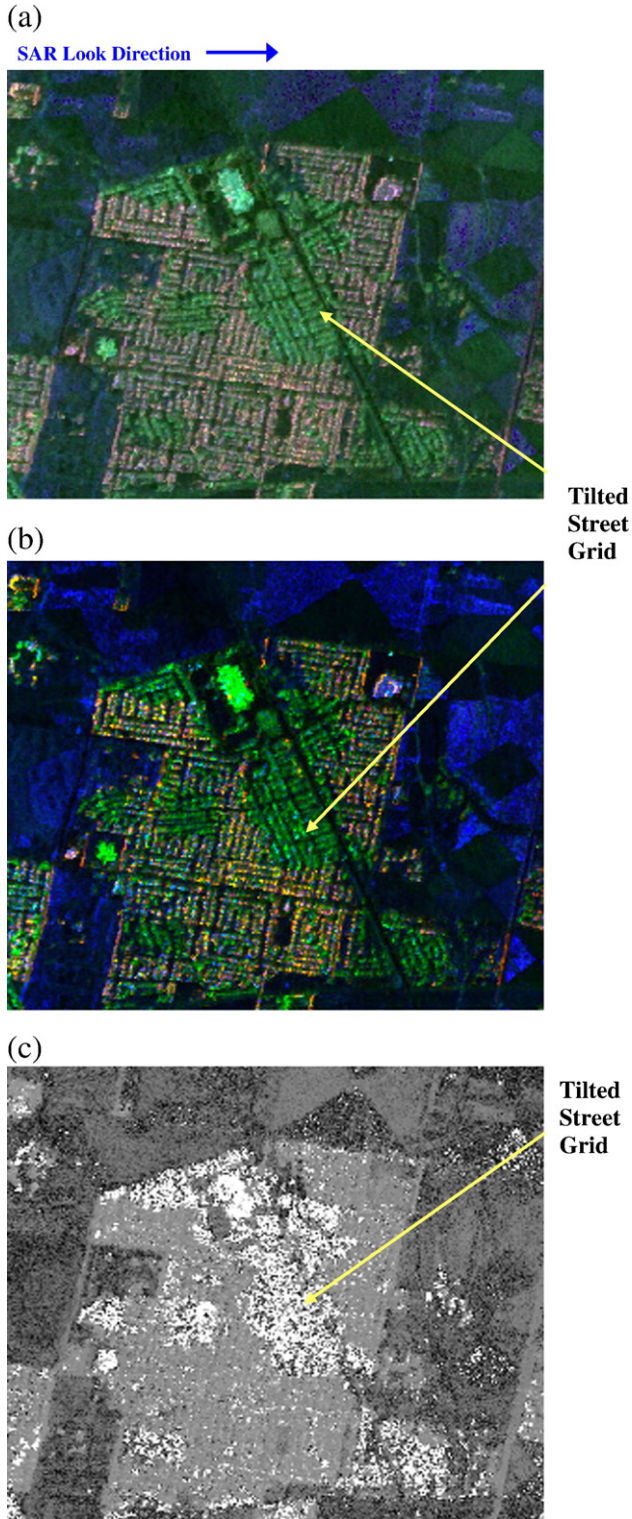


Fig. 1. Comparison of the Pauli decomposition (a) and the Freeman–Durden decomposition (b) of the study-site with an image of the ratio $|\rho|/|\rho_0|$, (c). Notice the section of buildings in the center of the study-site, which is tilted approximately 20° counter-clockwise from the vertical direction. This section appears green in (a) and (b), and white in the $|\rho|/|\rho_0|$ image. Green in both the Pauli display and the Freeman–Durden decomposition denotes strong $|HV|$, i.e. volume scattering. However, here the $|HV|$ returns arise from rotated dihedral scattering formed by reflections from the ground and the sides of rotated buildings.

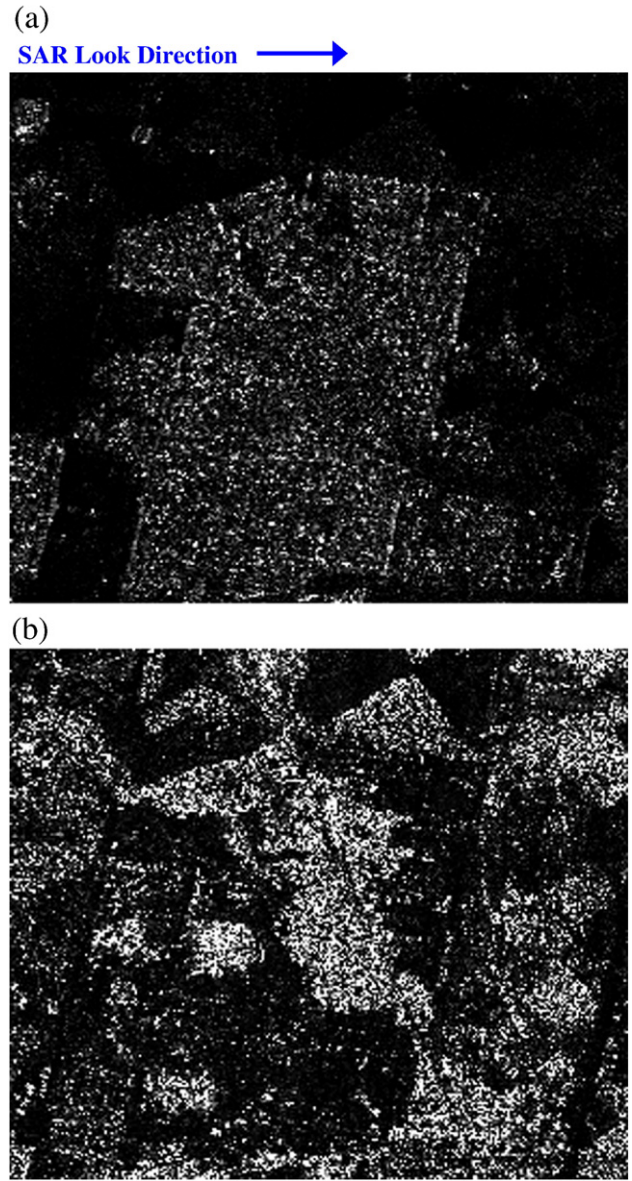


Fig. 2. Images of the study-site for the two major functional components of $|\rho|/|\rho_0|$. The image (a) shows the function $f(\tau)$, and (b) shows the function $g(\theta)$ of Eq. (14). Rotated buildings display strong orientation angle effects as do some surrounding agricultural areas of (b). The pattern of strong helical point scatterers neatly separates the urban and agricultural areas in (a).

The question remains as to whether, or not, the detection capability of $|\rho|/|\rho_0|$ significantly exceeds that of the helicity, τ , alone. To determine the relationship between $|\rho|/|\rho_0|$ and helicity, we considered the following:

- 1) The functional form $f(\tau)$ is mathematically a resonant pole (with $f(\pm 1) = \infty$) and the values of $f(\tau)$ will often far exceed one. Helicity, as manifested in $f(\tau)$, intensifies image urban features having high values of $|\tau|$. Non-azimuthally symmetric point scatterers embedded in an extensive natural area can be detected using $|\rho|/|\rho_0|$, since the sensitivity of $f(\tau)$ in the vicinity of the pole becomes quite large.
- 2) The component values of $|\rho|/|\rho_0|$ are both correlation functions that, by their definition, involve averaging. In the present study, the average is taken over twenty-five independent samples of the distribution of values. The function $f(\tau)$ is highly non-linear, especially near the location of the resonance. If the averaged samples show a RR/LL asymmetry then the value of τ will deviate

from zero and increase the $|\rho|/|\rho_0|$ value. For such cases a bright pixel will appear in the image.

- 3) The functional form of $|\rho|/|\rho_0|$ permits discrimination not only between urban and open, grassy areas, but also between these areas and forested areas. The functional dependence of $|\rho|/|\rho_0|$ on orientation angle θ is given by $g(\theta)=\sec(4\theta)$. The value of the orientation angle can come from azimuthal direction topography or from ground-wall scatter, or both. It can be evaluated using Eq. (6) and compensated for by dividing $|\rho|/|\rho_0|$ by $g(\theta)$. An example of individual variable sensitivities and the process of separating $f(\tau)$ and $g(\theta)$ is given later.

5. Polarimetric SAR applications using the normalization ($|\rho|/|\rho_0|$)

The polarimetric SAR image data described in this section has been used with the algorithm developed in the previous section to verify that localized scatterers from man-made structures, which do not have reflection-symmetric polarimetric scattering property, can be distinguished from distributed reflection-symmetric surface scatterers. It should be noted that man-made structures aligned along the azimuth direction also possess the property of reflection symmetry, however they can be easily distinguished because of double bounce scattering characteristics. Man-made structures not aligned in the azimuth direction introduce higher cross-pol returns, and do not have the reflection symmetry property. Their backscattered returns are difficult to distinguish from forest returns. The normalized ratio, $|\rho|/|\rho_0|$, can be applied to distinguish them. Examples are provided in the following to demonstrate this capability.

The data used for illustration in selected study-areas are L-band imagery acquired by either the NASA/AIRSAR operating from a DC-8 aircraft, or the German Experimental Synthetic Aperture Radar (E-SAR) L-band system on a Dornier DO-28 aircraft. Images were analyzed of, 1) Salt Lake City, Utah, 2) Dresden, Germany, 3) the Deutsche Forschungsanstalt für Luft und Raumfahrt (DLR) Facility at Oberpfaffenhofen, Germany, 4) Villingen-Schwenningen, Germany (Black Forest region, East of Freiburg), and 5) the Golden Gate Bridge, San Francisco, CA.

5.1. Study-Area 1: Salt Lake City (geometrical patterns of aligned houses)

A suburban housing community on the edge of Salt Lake City, Utah was chosen as a first study-area. A conventional Pauli decomposition image is given in Fig. 1a. In Fig. 1a blue pixels, proportional to $|S_{HH}+S_{VV}|^2$, are single bounce scatter events; red pixels, proportional to $|S_{HH}-S_{VV}|^2$, are double bounce events; and green pixels, proportional to $|S_{HV}|^2$, are volume scatter events. The radar look direction is from the left side of the image to the right side. Double bounce red pixels are, by themselves, a potential indicator of man-made structures. Double bounce scattering events can, however, originate from many natural situations. Among these situations are forest ground-trunk scattering interactions and scattering from abrupt, steep cliffs.

Details of these responses to building orientation are also apparent in the model-based Freeman-Durden decomposition (Freeman & Durden, 1998) image (Fig. 1b). In comparison the grey scale $|\rho|/|\rho_0|$ variations of Fig. 1c show distinct building orientations. The orientation angle (θ) is affected by both azimuth direction topography (Schuler et al., 1999, 2000) and the alignment of urban buildings (Kimura et al., 2004, 2005). The study-area topography is essentially flat; therefore, there is no contribution from the topography. In urban areas the largest values of $|\rho|/|\rho_0|$ (white-areas) occur when the building walls are not aligned in the along-track direction which then induces large values of θ . In Fig. 1c the clustered white areas contain buildings aligned up to $\sim 45^\circ$ away from the radar look direction. This explains the observed strong correlation between the (green) volume scattering areas in the Freeman–Durden image and the bright white areas of $|\rho|/|\rho_0|$. The Freeman–Durden volume scattering is defined by the strength of $|S_{HV}|^2$ covariance term, whereas a non-zero orientation angle in a region of urban double-bounce scattering induces a non-zero $|S_{HV}|^2$ term. Terrain slopes in the cross-range direction are also related analytically to changes in the polarimetric orientation angle and the SAR viewing geometry (Kimura et al., 2005). The study site in this example is, however, laid out on a nearly flat plain in the suburbs of Salt Lake City. Therefore, polarization orientation changes in this image occur due to urban building alignment changes relative to the azimuth direction.

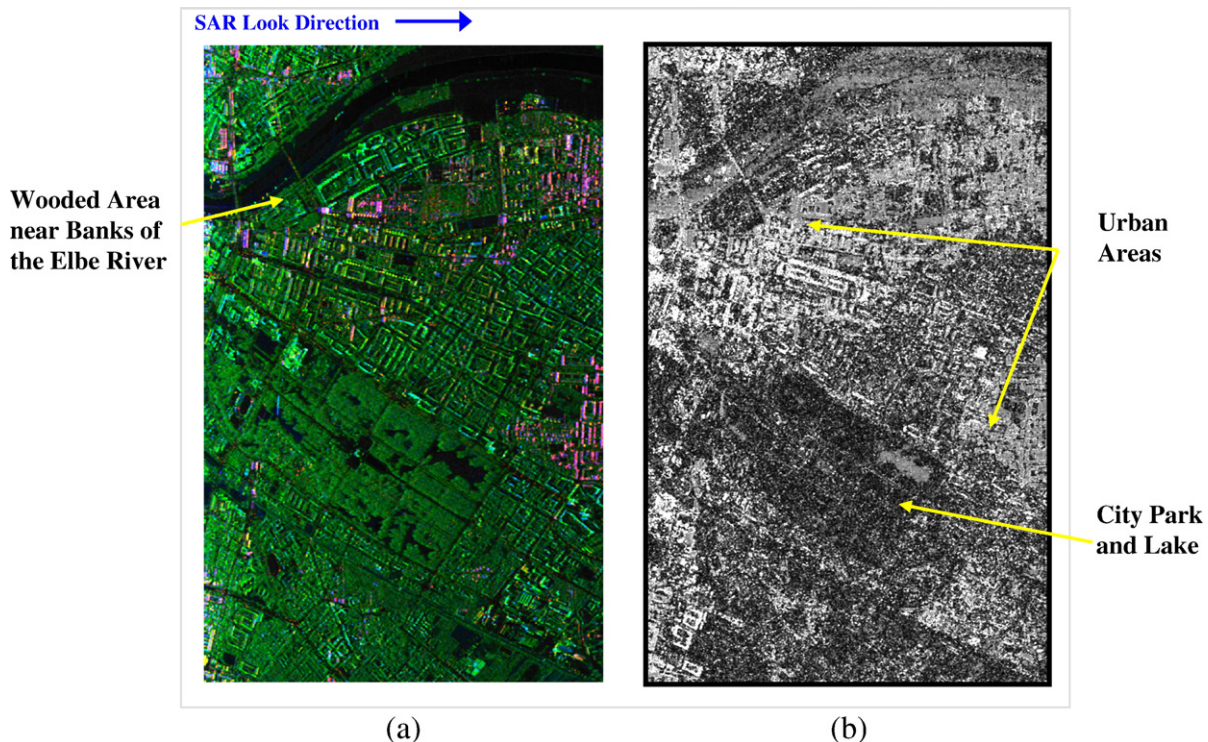


Fig. 3. ESAR images of Dresden, Germany. We show a Freeman–Durden image of central Dresden, Germany and the Elbe River in (a) and in (b) the $|\rho|/|\rho_0|$ image of the same area. Note the brightness of the urban areas relative to the darkness of forested areas in the city park and separate forested areas along the banks of the Elbe River at the top of the image.

Fig. 2a and b provide important examples of the separation of variables using study-site data and the functions $f(\tau)$ and $g(\theta)$ of Eq. (15). Fig. 2a gives $f(\tau)$ and Fig. 2b gives $g(\theta)$ for the study site. Values of θ and τ were calculated from Eqs. (6) and (12), respectively. In Fig. 2a, the urban areas are cleanly separated from the surrounding vegetation; vegetation typically has low helicity and high $|S_{HV}|^2$ unlike the urban areas that display both non-zero helicity and $|S_{HV}|^2$. Fig. 2b shows orientation angle effects in both urban and natural areas, though the effects are stronger in urban areas. For cases

where terrain slopes are known, the orientation angles θ should be corrected for the scene topography prior to estimating the $|\rho|/|\rho_0|$ ratio. This ability to compensate for terrain slope effects is important for urban areas; e.g., San Francisco, that have significant terrain azimuth slopes.

The helicity and orientation angle values and patterns are consistent with the presence of man-made street-grids and structures. Buildings having faces that are aligned in the perpendicular (azimuth) direction are darker; i.e., have low $|\rho|/|\rho_0|$.

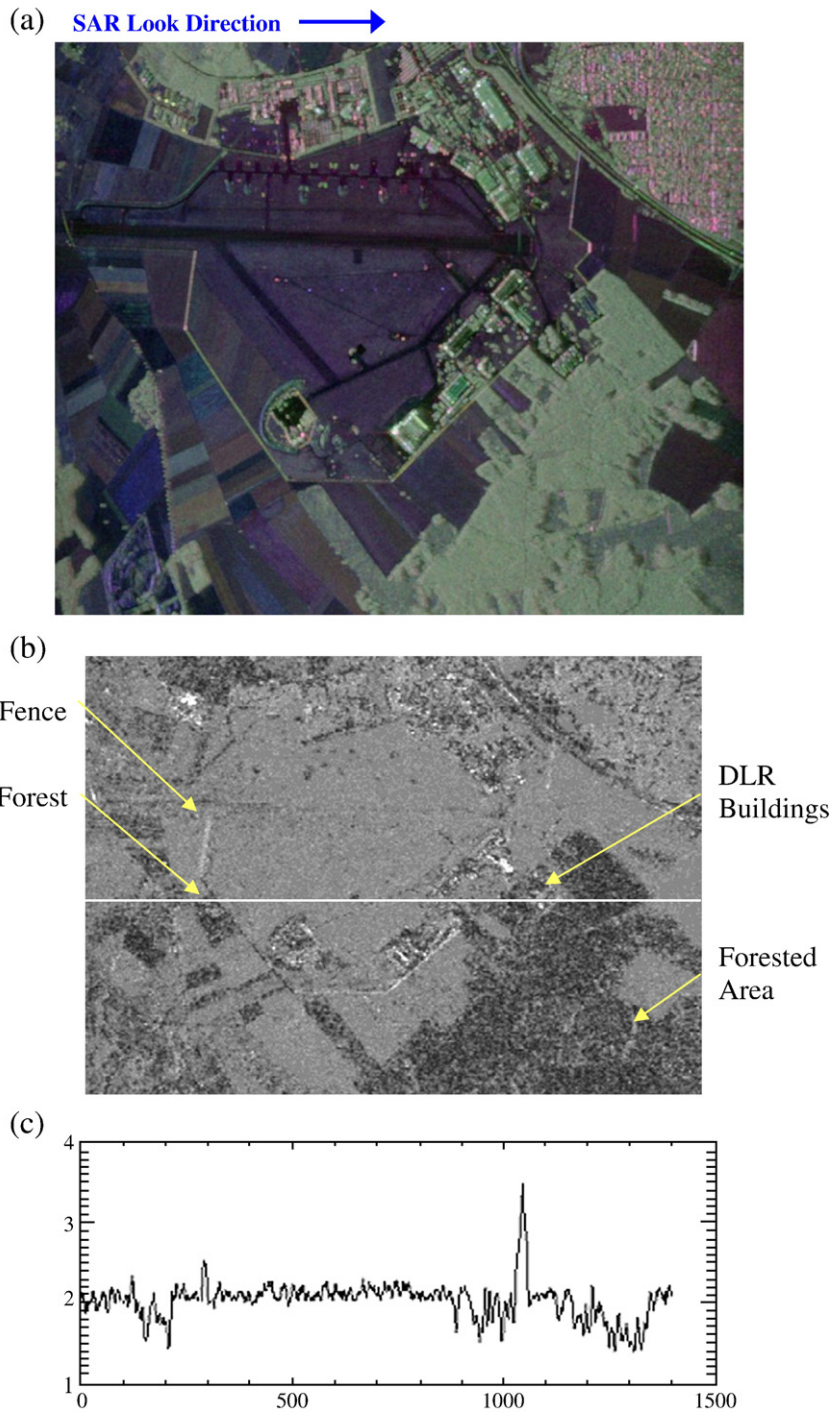


Fig. 4. Pauli decomposition image, (a), of the study-site DLR facilities at Oberpfaffenhofen, Germany. The blue areas are dominated by single-bounce surface, or grass, backscatter. The red areas are dominated by double-bounce backscatter from man-made structures. The green areas are volume backscatter from forest canopy. The black linear patterns are DLR airport runways with low backscatter from their smooth surfaces. The $|\rho|/|\rho_0|$ image is shown in (b). This facility contains buildings surrounding an airfield for research aircraft. A profile of 5x5 averaged values of the ratio $|\rho|/|\rho_0|$ versus pixel number along the white line shown in (b) is given in (c). Note that the resonant structure scatter is >2 , the field scatter ratio is ~ 2.0 , and the dark forested areas are <2 .

Buildings aligned at up to 45° from this direction are bright; i.e., have high $|\rho|/|\rho_0|$. In a recent study, Kimura et al. (2004) have shown that orientation angle changes can result when double bounce scattering occurs between the ground and the vertical walls of buildings. Non-zero values occur when the wall is not aligned with the SAR cross-range flight direction. This figure shows the separate effects of the orientation angle and the helicity on $|\rho|/|\rho_0|$ of Eq. (11).

5.2. Study-Area 2: Dresden, Germany (discrimination between urban, open and forest areas)

A DLR ESAR L-band image taken of Dresden, Germany and the normalization algorithm show the potential of the method to discriminate between densely urbanized areas and natural open terrain in park areas (Fig. 3). The Freeman–Durden decomposition is shown in Fig. 3a and the $|\rho|/|\rho_0|$ image in Fig. 3b is given for an area near the center of the restored city. In the lower-left of the image is a large, rectangular, city park that is heavily wooded. Dense clusters of buildings surround the park. In the upper part of the image forested park areas line the banks of the Elbe River. In a conventional VV or HH image of the area, both the forest areas and the urban areas produce strong intensity images. The normalized $|\rho|/|\rho_0|$ images of the same area have urban $|\rho|/|\rho_0|$ considerably above a value of 2.0, grassy areas ≈ 2.0 , and forested area backscatter which tends to be < 2.0 . Thus, segmentation of these areas becomes possible.

5.3. Study-Area 3: DLR Facility Oberpfaffenhofen, Germany (buildings, fields and forests)

A polarimetric L-band ESAR image of the German DLR Facility located at Oberpfaffenhofen, Germany is used as an example in Fig. 4. The Oberpfaffenhofen scene incorporates a variety of scatterers: open fields, forests, urban areas, and other man-made structures. Fig. 4a is a conventional Pauli decomposition image. The areas in the center are grassy fields (blue) and airport runways (darker, black). The areas around the perimeter are forested (green). The DLR buildings have strong responses and many are double bounce (red). In the image (Fig. 4b) the ratio $|\rho|/|\rho_0|$ is shown. The localized scattering resonances (values much greater than 1) are caused by scatter from known buildings in the DLR complex. The surface scatter (values near 2) is light grey, and heavily wooded areas (values less than 2) are dark grey to black (Fig. 4b). The profile given in Fig. 4c indicates that a significant resonance in $|\rho|/|\rho_0|$ is obtained when scatter from DLR facility buildings occurs. In addition, the separation of open grassy areas from known forested areas on the perimeter of the DLR grounds is well defined. The $|\rho|/|\rho_0|$ image and the Pauli decomposition are fundamentally in agreement.

5.4. Study-Area 4: Black Forest, Germany (localized scatterers in forests and meadows)

The Villingen–Schwenningen / Black Forest images (Figs. 5 and 6) contain urban-like small town areas, forested areas, and also, open

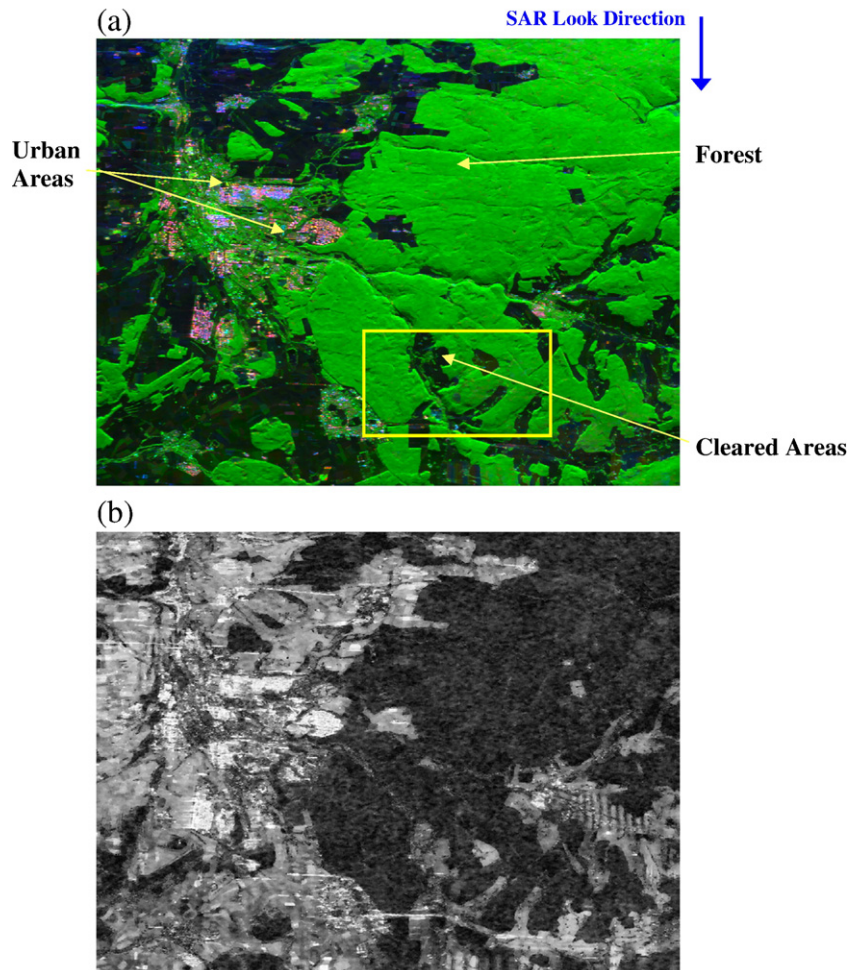


Fig. 5. Villingen–Schwenningen, Germany: (a) The Freeman–Durden decomposition image with red for double-bounce, green for volume and blue for surface scattering; (b) Conventional RRL circular-pol $|\rho|$ image of urban and natural areas. The yellow box denotes the region of interest shown in Fig. 6.

grassy areas. Fig. 5a is an image created using the Freeman–Durden decomposition (Freeman & Durden, 1998). Areas with surface (odd bounce) scatter are colored blue, even bounce is red and volume scatter is colored green. Backscatter from complex structures in urban areas is often dominated by double bounce scattering. Fig. 5b shows the magnitude of the conventional circular-pol RR-LL correlation coefficient, $|\rho|$. Light areas are well correlated and dark areas are decorrelated. The image contains a great deal of information about correlation levels, but for detecting localized targets it is complicated.

Fig. 6 gives a comparison of the Freeman–Durden image (Fig. 6a) and the $|\rho|/|\rho_0|$ image (Fig. 6b) of the region of interest denoted by Fig. 5a. The $|\rho|/|\rho_0|$ image was calculated explicitly from $|\rho|$ and $|\rho_0|$, but could have been calculated using Eq. (11). The white localized scatterers in region of interest are much brighter than the ambient background. Trails of some of the bright points seem to follow known roads through the Black Forest. Others are distributed throughout the open areas. The exact nature of the bright scatterers shown in the $|\rho|/|\rho_0|$ image is not known. Local topography may induce some of the

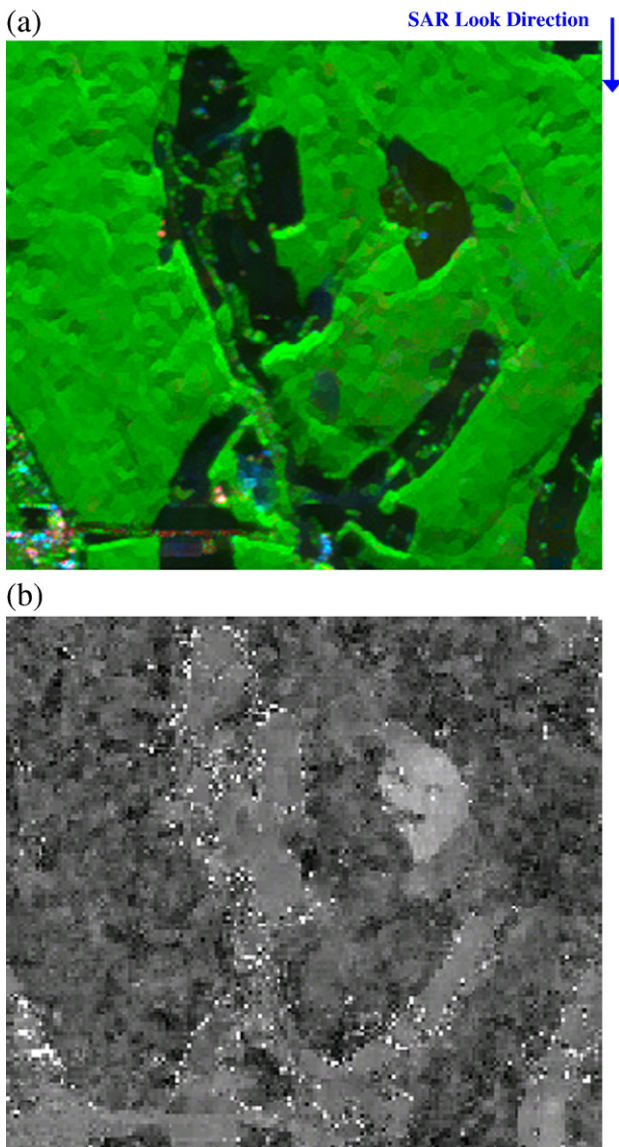


Fig. 6. Comparison of the Freeman–Durden decomposition (a) with the normalized $|\rho|/|\rho_0|$ correlation coefficient image (b). A mixture of odd-bounce (dark-blue), even-bounce (red) and volume scatter (green) scattering events can be compared with the $|\rho|/|\rho_0|$ bright localized returns.

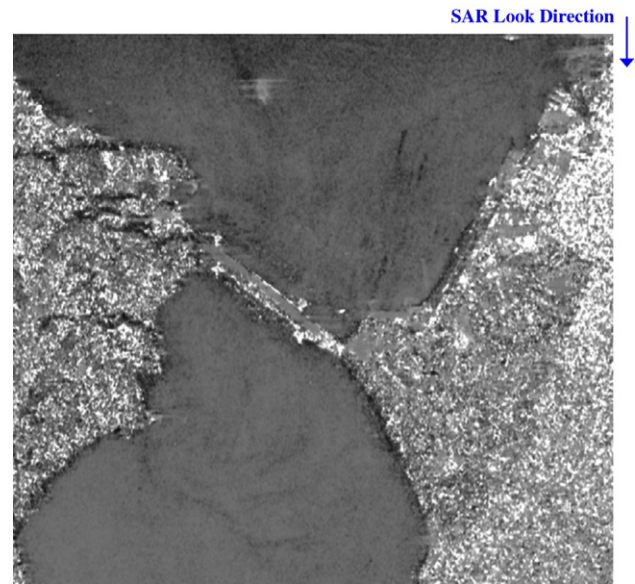


Fig. 7. This figure shows the area surrounding the Golden Gate Bridge and the city of San Francisco (L-band NASA/AIRSAR data). Note the returns from the bridge towers/railings and the lower density of singular points and correlation in the more open-land of the former Presidio Base. The concentration of high $|\rho|/|\rho_0|$ responses on the right (below and to the right of Golden Gate Park) is due to urban structures. The responses to the left of the bridge are due to orientation angle shifts caused by rugged, rocky, slopes of the Marin County headlands.

strong $|\rho|/|\rho_0|$ responses via double bounce scattering from sloped ground and tree trunks. However, the strong $|\rho|/|\rho_0|$ responses do not appear along all forest-field boundaries. These localized targets are much more detectable in the $|\rho|/|\rho_0|$ image for both single and double bounce scattering events.

5.5. Study-Area 5: Golden Gate Bridge, San Francisco, CA (detection of urban structures)

An urban example, given in Fig. 7, shows (L-band NASA/AIRSAR data) the area surrounding the Golden Gate Bridge and a northern portion of the city of San Francisco. Note the intense resonant localized $|\rho|/|\rho_0|$ returns from the Golden Gate bridge towers / railings, and also the lower density of singular points and darker gray in the more open-land natural areas of the former Presidio Base. The concentration of bright white responses on the upper right is due to urban structures in downtown San Francisco. The lower density of bright responses (on the left side of the image) are due to complex scatter from the rugged, rocky slopes of the Marin County headlands located on the north shore of the bridge span. Thus, for regions with significant local topographic slopes the orientation angle (θ) can generate a strong $|\rho|/|\rho_0|$ response.

6. Conclusions

A method has been investigated which shows potential for detecting and enhancing the suitably processed SAR returns from non-reflection symmetric features. This type of feature is often characteristic of man-made structures. By creating circular polarization correlation coefficients ($|\rho|$, $|\rho_0|$) and then forming the ratio, $|\rho|/|\rho_0|$, the method 1) normalizes its value from natural surface areas (reflection symmetric) to one, and 2) significantly enhances signals from man-made structures (scatterers without reflection symmetry) allowing them to be detected more easily. Urban areas also may be separated from surrounding forested areas by their higher helicity, τ , values. A singularity, or resonant pole, in the helicity, τ , response of $|\rho|/|\rho_0|$ allows its response values to have gains

significantly greater than one. The non-linear amplification of responses from high helicity structures is the most important contribution of this work. Man-made structures in urban settings tend to have higher helicity values which are amplified the most, whereas, natural settings have low helicity values which are amplified least.

The separable contribution to $|\rho|/|\rho_0|$ of the orientation angle, θ , is due to both topography and, in urban areas, building alignments. The expression $|\rho|/|\rho_0|$ allows both helicity and orientation angles to be calculated independently (e.g., Fig. 2) and used in established classification algorithms.

Finally, variations in image intensity due to changes in natural terrain small-scale surface roughness are greatly reduced by the ratio $|\rho|/|\rho_0|$. The normalized $|\rho|/|\rho_0|$, therefore, provides strong return from scattering situations with high helicity, and smoothes image detail due to surface roughness variations.

Appendix A

Scattering from helical targets has usually been discussed in connection with coherent decompositions of target scattering matrices, e.g. (Cameron et al., 1996; Huynen, 1965; Krogager et al., 1998; Touzi, 2007; Touzi & Charbonneau 2002). Helical backscattering may result either directly from helical targets, or indirectly from a coherent superposition of non-helical scatterers. For example, the coherent returns from a pair of dihedral targets rotated 45° with respect to one another and offset in range by $\lambda/8$ generates a purely helical response (Ulaby & Elachi, 1990). Our development follows Krogager et al. (1998) and the subsequent extension to eigenvector / eigenvalue decompositions of the circular-basis covariance matrix by Ainsworth et al. (2002). Starting with Krogager's sphere–diplane–helix decomposition of the scattering matrix in the circular basis (Krogager et al., 1998) we consider the scattering matrix for a target with a left wound helix return.

$$\begin{aligned} [S] &= \begin{bmatrix} S_{RR} & S_{RL} \\ S_{LR} & S_{LL} \end{bmatrix} = e^{i\varphi} \left\{ k_s e^{i\phi_s} \begin{bmatrix} 0 & i \\ i & 0 \end{bmatrix} + k_d \begin{bmatrix} e^{i2\theta} & 0 \\ 0 & -e^{-i2\theta} \end{bmatrix} + k_h \begin{bmatrix} e^{i2\theta} & 0 \\ 0 & 0 \end{bmatrix} \right\} \\ &= e^{i\varphi} \begin{bmatrix} (k_d + k_h)e^{i2\theta} & ik_s e^{i\phi_s} \\ ik_s e^{i\phi_s} & -k_d e^{-i2\theta} \end{bmatrix} \end{aligned} \quad (A1)$$

where the strengths of the sphere, diplane and helical returns are k_s , k_d and k_h , respectively. The two angles θ and ϕ_s are the orientation angle, and relative phase between surface and dihedral scattering. The relative magnitudes of $|S_{RR}|$ and $|S_{LL}|$ determine the choice between a left-handed or right-handed helix in Eq. (A1); $k_d = \min(|S_{RR}|, |S_{LL}|)$, $k_h = ||S_{RR}| - |S_{LL}||$. Eq. (A1) explicitly displays the case where $|S_{RR}| \geq |S_{LL}|$. The covariance matrix formed from Eq. (A1) in the circular basis becomes

$$[C] = \begin{bmatrix} (k_d + k_h)^2 & -i\sqrt{2}k_s(k_d + k_h)e^{-i(\phi_s - 2\theta)} & -k_d(k_d + k_h)e^{i4\theta} \\ i\sqrt{2}k_s(k_d + k_h)e^{i(\phi_s - 2\theta)} & 2k_s^2 & -i\sqrt{2}k_d k_s e^{i(\phi_s + 2\theta)} \\ -k_d(k_d + k_h)e^{-i4\theta} & i\sqrt{2}k_d k_s e^{-i(\phi_s + 2\theta)} & k_d^2 \end{bmatrix} \quad (A2)$$

Scattering from a pure left-handed helical target, i.e. $k_s = k_d = 0$, generates only one non-zero circular-basis covariance matrix element, $|S_{RR}|^2$; similarly, for a pure right-handed helical target only $|S_{LL}|^2$ is non-zero (Krogager et al., 1998; Ulaby & Elachi, 1990). The return from a dihedral may equivalently be written as the coherent sum of two equal strength helices: one left-handed, the other right-handed. In this case $|S_{RR}|^2 = |S_{LL}|^2$, and there is no RR / LL asymmetry. Therefore the difference between $|S_{RR}|^2$ and $|S_{LL}|^2$ measures the relative strengths of right-handed versus left-handed helical scattering.

The eigen decomposition of the circular basis covariance matrix (Ainsworth et al., 2002) relates the asymmetry between $|S_{RR}|^2$ and $|S_{LL}|^2$

to the eigenvector parameter θ_τ that characterizes the helicity of the dominant eigenvector. Without loss of generality, the co-pol terms of Eq. (A2) reduce to

$$\begin{aligned} &\begin{bmatrix} (k_d + k_h)^2 & \cdots & k_d(k_d + k_h)e^{i(4\theta + \pi)} \\ \cdots & \cdots & \cdots \\ k_d(k_d + k_h)e^{-i(4\theta + \pi)} & \cdots & k_d^2 \end{bmatrix} \\ \alpha &\begin{bmatrix} \cos^2(\theta_\tau) & \cdots & \cos(\theta_\tau)\sin(\theta_\tau)e^{i(4\theta + \pi)} \\ \cdots & \cdots & \cdots \\ \cos(\theta_\tau)\sin(\theta_\tau)e^{-i(4\theta + \pi)} & \cdots & \sin^2(\theta_\tau) \end{bmatrix} \end{aligned} \quad (A3)$$

where $\cos^2(\theta_\tau) \equiv \frac{(k_d + k_h)^2}{(k_d + k_h)^2 + k_d^2}$, $\sin^2(\theta_\tau) \equiv \frac{k_d^2}{(k_d + k_h)^2 + k_d^2}$ and the ellipses refer to the circular cross-pol covariance terms that do not affect the following discussion. From a covariance matrix that represents a single scattering mechanism we derive the exact relationship

$$\cos(2\theta_\tau) = \cos^2(\theta_\tau) - \sin^2(\theta_\tau) = \frac{(k_d + k_h)^2 - k_d^2}{(k_d + k_h)^2 + k_d^2} = \frac{|S_{RR}|^2 - |S_{LL}|^2}{|S_{RR}|^2 + |S_{LL}|^2} \quad (A4)$$

Eq. (A4) provides the explicit connection between the Krogager et al. (1998) k_d and k_h scattering matrix parameters, the eigenvector parameterization, i.e. θ_τ , of the circular basis covariance matrix (Ainsworth et al., 2002), and the $|S_{RR}|^2$ and $|S_{LL}|^2$ elements of the covariance matrix. In fact, only helical scattering generates RR / LL asymmetries in the covariance matrix. We derived Eq. (A4) assuming $|S_{RR}| \geq |S_{LL}|$ which limits the range of θ_τ to $[0^\circ, 45^\circ]$. The case where $|S_{LL}| \geq |S_{RR}|$ follows similarly; however the range of θ_τ becomes $[45^\circ, 90^\circ]$. Combining the results for all values of $|S_{RR}|$ and $|S_{LL}|$, for the full range of θ_τ , $[0^\circ, 90^\circ]$, yields

$$\cos(2\theta_\tau) = \frac{|S_{RR}|^2 - |S_{LL}|^2}{|S_{RR}|^2 + |S_{LL}|^2} \quad (A5)$$

Eigen decompositions represent general covariance matrices as an incoherent summation of three mutually orthogonal scattering mechanisms. For covariance matrices composed of multiple scattering mechanisms, we consider the mean helicity, τ , which is parameterized by $\bar{\theta}_\tau$ and defined by the averaged covariance matrix elements as in Eq. (A6).

$$\tau = \cos(2\bar{\theta}_\tau) = \frac{\langle |S_{RR}|^2 \rangle - \langle |S_{LL}|^2 \rangle}{\langle |S_{RR}|^2 \rangle + \langle |S_{LL}|^2 \rangle} \quad (A6)$$

This is Eq. (12) in the text. This measure of the covariance matrix RR/LL asymmetry naturally arises in Eq. (11) for $|\rho|/|\rho_0|$. In this Appendix, we developed the connection between helical scattering and the RR/LL asymmetries of the covariance matrix.

References

- Ainsworth, T. L., Cloude, S. R., & Lee, J. -S. (2002). Eigenvector analysis of polarimetric SAR data. *Proc. IEEE Int. Geosci. Remote Sens. Sym. (IGARSS 2002)*. Toronto, Canada (pp. 626–628).
- Cameron, W. L., Youssef, N. N., & Leung, L. K. (1996). Simulated polarimetric signatures of primitive geometric shapes. *IEEE Transactions on Geoscience and Remote Sensing*, 34, 793–804.
- Freeman, A., & Durden, S. (1998). A three-component scattering model for polarimetric SAR data. *IEEE Transactions on Geoscience and Remote Sensing*, 36, 963–973.
- Huynen, J. R. (1965). Measurement of the target scattering matrix. *Proceedings of ... IEEE*, 34, 936–946.
- Kasilingam, D., Schuler, D. L., & Lee, J. -S. (2001). The depolarization of radar backscatter from rough surfaces due to surface roughness and slopes. *Proc. IEEE Int. Geosci. Remote Sens. Sym. (IGARSS 2001)*. Sydney, Australia (pp. 925–927).
- Kimura, K., Yamaguchi, Y., Moriyama, T., & Yamada, H. (2004). Circular polarization correlation coefficient for detection of non-natural targets aligned not parallel to SAR flight path in the x-band POLSAR image analysis. *IEICE Transactions on Communications*, E87-B, 3050–3056.
- Kimura, H., Papathanassiou, K., & Hajnsek, I. (2005). Polarization orientation effects in urban areas on SAR data. *Proc. IEEE Int. Geosci. Remote Sens. Sym. (IGARSS 2005)*. Seoul, Korea (pp. 4863–4867).

- Krogager, E., Cloude, S. R., Lee, J. -S., Ainsworth, T. L., & Boerner, W. -M. (1998). Interpretation of high resolution polarimetric SAR data. *Proc. 4th Int. Workshop on Radar Pol.* Nantes, France (pp. 165–170).
- Lee, J. -S., Schuler, D. L., & Ainsworth, T. L. (2000). Polarimetric SAR data compensation for azimuth slope variation. *IEEE Transactions on Geoscience and Remote Sensing*, 38, 2153–2163.
- Lee, J. -S., Schuler, D. L., Ainsworth, T. L., Krogager, E., Kasilingam, D., & Boerner, W. -M. (2002). On the estimation of radar polarization orientation shifts induced by terrain slopes. *IEEE Transactions on Geoscience and Remote Sensing*, 40, 30–41.
- Mattia, F., Le Toan, T., Souyris, J. -C., De Carolis, G., Floury, N., & Posa, F. (1997). The effect of surface roughness on multifrequency polarimetric SAR data. *IEEE Transactions on Geoscience and Remote Sensing*, 35, 954–966.
- Schuler, D. L., Lee, J. -S., & Ainsworth, T. L. (1999). Compensation of terrain azimuthal slope effects in geophysical parameter studies using polarimetric SAR data. *Remote Sensing of Environment*, 69, 139–155.
- Schuler, D. L., Lee, J. -S., & Ainsworth, T. L. (2000). Terrain topography measurement using multi-pass polarimetric SAR data. *Radio Science*, 35, 812–832.
- Schuler, D. L., Lee, J. -S., & De Grandi, G. (2006). Characteristics of polarimetric SAR scattering in urban and natural areas. *Proc. European SAR Conference (EUSAR 2006)*. Dresden, Germany.
- Schuler, D. L., Lee, J. -S., & Ainsworth, T. L. (2006). Polarimetric SAR detection of man-made structures using normalized circular-pol correlation coefficients. *Proc. IEEE Int. Geosci. Remote Sens. Sym. (IGARSS 2006)*. Denver, Colorado (pp. 485–488).
- Touzi, R. (2007). Target scattering decomposition in terms of roll-invariant target parameters. *IEEE Transactions on Geoscience and Remote Sensing*, 45, 73–84.
- Touzi, R., & Charbonneau, F. (2002). Characterization of target symmetric scattering using polarimetric SARs. *IEEE Transactions on Geoscience and Remote Sensing*, 40, 2507–2516.
- Ulaby, F. T., & Elachi, C. (1990). *Radar Polarimetry for Geoscience Applications*. Norwood, Massachusetts: Artech House.